ACSNANO

www.acsnano.org

ARTICLE

Oblique Colloidal Lithography for the Fabrication of Nonconcentric Features

Zhi Zhao,[†,⊥] Yang Cao,[§] Yangjun Cai,[‡] Jian Yang,[§] Ximin He,[⊥] Peter Nordlander,[§] and Paul S. Cremer*[,†,‡]

[†]Department of Chemistry, Texas A&M University, College Station, Texas 77843, United States

[‡]Department of Chemistry and Department of Biochemistry and Molecular Biology, Penn State University, University Park, Pennsylvania 16803, United States

[§]Department of Physics and Astronomy, Rice University, Houston, Texas 77251, United States

[⊥]School for Engineering of Matter, Transport and Energy, Arizona State University, 781 E. Terrace Road, Tempe, Arizona 85287, United States

Supporting Information

ABSTRACT: **Herein, we describe the development of oblique colloidal lithography (OCL) and establish a systematic patterning strategy for creating libraries of nanosized nonconcentric plasmonic structures. This strategy combines OCL, capillary force lithography, and several wet and ion etching steps. Hexagonal arrays of nonconcentric gold features were created on glass substrates with highly controllable geometric parameters. The size, geometry, and eccentricity of the gold features could be independently tuned by controlling the experimental conditions. Gaps within surface elements could be shrunk to as small as 30 nm, while the total patterned area was about 1 cm^2. The goal was to devise a method that offers a high degree of control over the resolution and morphology of asymmetric structures without the need to resort to electron beam lithography. This technique also enabled the development of numerous surface patterns through the stepwise fabrication of separate elements. Complex features, including dots-surrounded nonconcentric targets, nonconcentric hexagram-disks, and nonconcentric annular aperture arrays, were demonstrated, and their optical properties were characterized. Indeed, spectroscopic studies and FDTD simulations demonstrated that Fano resonances could readily be generated by the nonconcentric gold features. Consequently, our patterning strategy should enable the high-throughput investigation of plasmonic coupling and Fano resonances as a function of the physical parameters of the elements within the nanopattern array.**

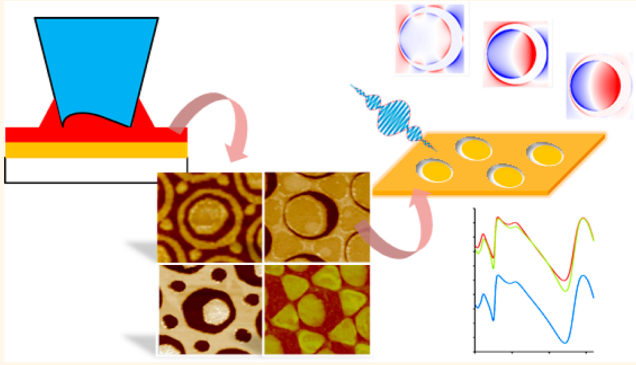

KEYWORDS: *oblique colloidal lithography, stepwise fabrication, surface plasmon, symmetry breaking, multipolar resonance*

The collective oscillation of conduction electrons supported at a metallic interface is known as a surface plasmon.[1] The local electromagnetic field of metallic structures is significantly enhanced at the frequency corresponding to the surface plasmon resonance (SPR), which depends on the chemical and geometric characteristics of the nanostructures. Great potential exists for the application of plasmonic devices to the fields of photonics,[2,3] electronics,[4] material science,[5] and biotechnology.[6−11] The optical properties of any given metallic nanostructure are highly dependent on its size and geometry.[12−15] As a result, it is desirable to develop patterning techniques that are capable of creating libraries of surface structures for obtaining the most efficient geometries for a given individual purpose.

Recently, fabrication strategies and SPR properties of asymmetric patterns have been demonstrated by several research groups.[16−18] Optical applications of nanosystems should benefit from the breaking of symmetry because this will create more spectrally observable SPRs. It is well known that plasmonic resonances can be classified as either bright modes or dark modes according to their coupling efficiency with an external electromagnetic field.[19] In contrast to bright modes, which possess a finite dipolar moment, the charge distribution for dark mode SPR resonances possesses a center

Received: November 22, 2016
Accepted: July 3, 2017
Published: July 13, 2017

 © 2017 American Chemical Society

DOI: 10.1021/acsnano.6b07867
ACS Nano 2017, 11, 6594−6604

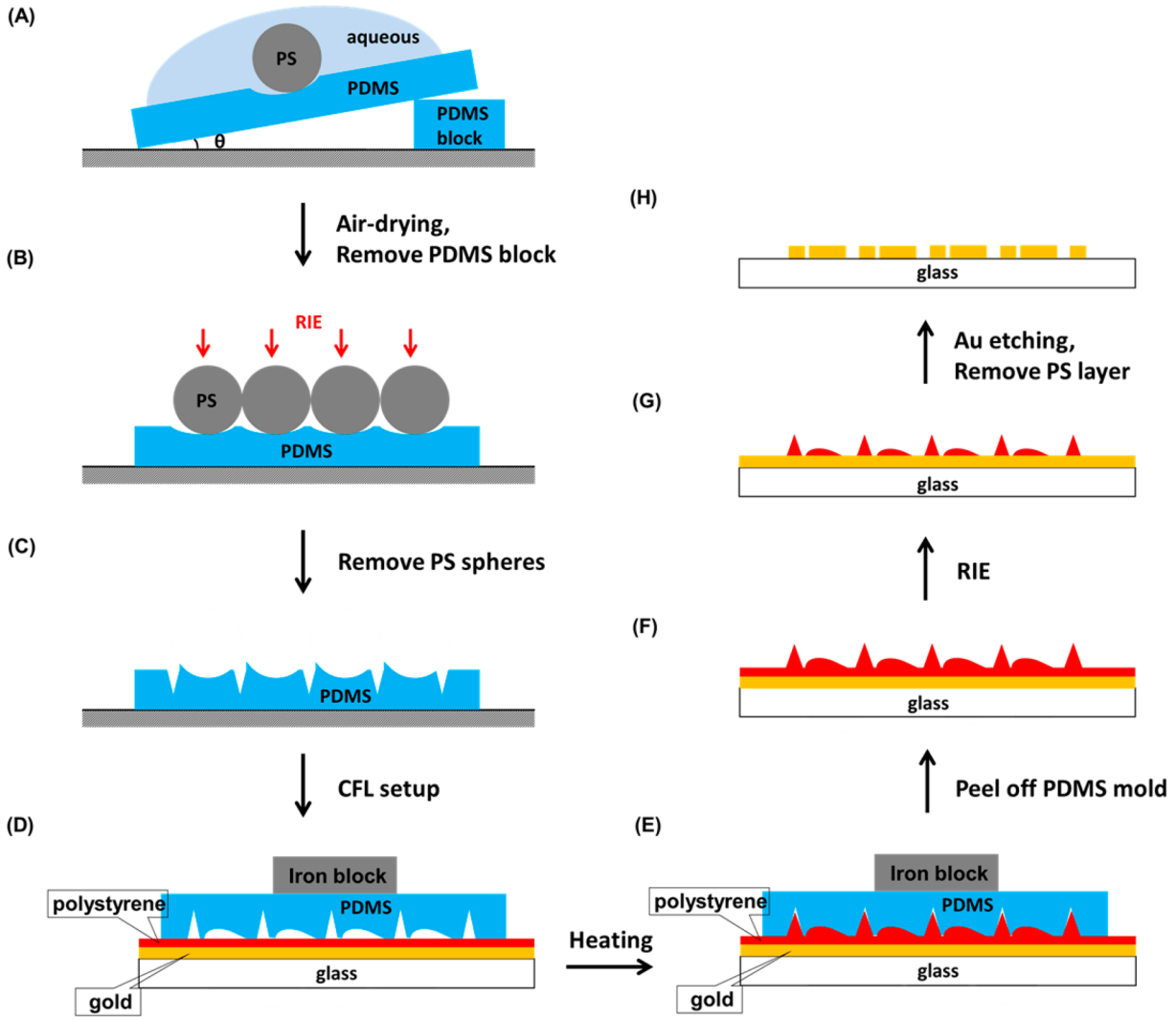

Figure 1. Schematic illustration of the patterning steps involved in the fabrication of nonconcentric gold nanofeatures. Note: In step (a), the PS sphere-layer-covered PDMS surface was allowed to cure at room temperature for 24 h to cure the interfacial PDMS oligomers and thereby lock the asymmetric pattern into place.

of symmetry and has no net dipolar moment, which prevents its coupling to the electric field of light.[20] In most cases, the center of the charge distribution coincides with the geometric center of the nanostructure. Therefore, to render the dark modes visible, the inversion symmetry of the structure must be removed. Such asymmetric structures typically exhibit several bright modes. This is important because the excitation of multiple SPR modes increases the number of resonances that could potentially be employed in sensing applications. Indeed, this type of multifrequency behavior is highly desirable for potential applications in the spectroscopic detection of chemical or biochemical analytes and the phase imaging of materials that show distinct absorptions or "fingerprints" at multiple frequencies.[21,22]

The appearance of Fano resonances is a distinctive feature of asymmetric plasmonic structures. Fano resonances typically exhibit distinctly asymmetric spectral profiles that originate from the constructive and destructive interference of narrow dark resonances with broad bright resonances.[23] The appearance of plasmonic Fano resonances typically requires structural symmetry breaking.[24] Several examples of Fano resonances have been demonstrated in plasmonic materials and metamaterials.[16,18,25] Compared to normal plasmon modes, Fano resonances possess much narrower peak widths and respond to environmental changes more sensitively[26] and, therefore, can lead to lower detection limits.[27] Therefore, asymmetric features with Fano resonances should be promising candidates for the design of better biosensors. In addition, the optical behavior of Fano resonances, including plasmon-induced transparency[28] and polarization-dependent transmittance,[18] could potentially be integrated into optical or electronic devices.[29]

At present, the majority of asymmetric nanostructures are fabricated by electron beam lithography (EBL)[30−32] due to the requirement of a high degree of control over geometry and morphology. Indeed, the more complicated the nanostructure is, the harder it typically is to create it without using EBL. Although a few alternative methods have been developed to fabricate asymmetric plasmonic structures,[33,34] they are only applicable to very simple geometries. At present, planar nonconcentric structures consisting of two or more geometric units and a mismatch in their geometric centers can be created only by EBL. While it is possible to fabricate almost any arbitrary feature with 10 nm resolution or better by EBL, the

DOI: 10.1021/acsnano.6b07867
ACS Nano 2017, 11, 6594−6604

time and cost for making patterns rises tremendously as the patterned area increases and the features become more complicated. In addition, the symmetry breaking needed for the features that are generally employed is typically very large (hundreds of nanometers).[17,26,29] At these larger length scales, colloidal lithography (CL)[35,36] offers a considerable advantage over EBL. CL is a simple, cost-effective method that generally meets the resolution, large-area, cost, and time requirements for fabrication. Numerous structures, such as disks,[37,38] circular rings,[39−42] triangles,[35] and crescents,[43] have been generated at the nanoscale using spherical colloids as templates. Recent developments in CL have made it possible to create complex surface features with precisely controlled geometry.[44,45] Some of the features can give rise to Fano resonances.[46,47] Unfortunately, however, CL has not yet been shown to possess the ability to create planar nonconcentric patterns because of the intrinsic symmetry of the colloidal particles being employed. Therefore, there are still existing challenges for designing alternative techniques to achieve fine resolution and complex nonconcentric features over macroscopic areas in a reasonable time period.

Herein, we demonstrate an inexpensive strategy to overcome the problem of nanofeature fabrication to generate libraries of symmetry-breaking structures over large areas with high resolution for individual elements. A versatile technique, dubbed oblique colloidal lithography (OCL), is developed to fabricate polydimethylsiloxane (PDMS) templates with asymmetric contours, which allow us to create nonconcentric polymer features. Control over surface units with high resolution is realized by reactive ion etching, imprint molding, and capillary force lithography (CFL).[48] By conducting a wet chemical etching step, each polymer feature can be transferred to a metal film for the production of plasmonic structures. This method is capable of realizing a high level of control over nonconcentric nanofeatures without using EBL. A significant advantage of this technique also stems from its stepwise nature. Stepwise patterning allows the user to create an exponentially increasing variety of patterns. In fact, multiple types of features can be created from a single starting structure by tuning the experimental conditions at each patterning step.

RESULTS AND DISCUSSION

Fabrication of Nonconcentric Plasmonic Structures. Figure 1 shows a schematic diagram of the procedures used to fabricate nonconcentric plasmonic structures. First, a self-assembled monolayer (SAM) of polystyrene (PS) spheres was deposited onto a tilted PDMS block (Figure 1A). To do this, a flat PDMS substrate was first made and rendered hydrophilic in an O_2 plasma. Next, PS spheres were deposited from an aqueous suspension onto the tilted planar PDMS surface.[49−52] Prior to deposition, the PS spheres were centrifuged, washed, and diluted to a concentration of 4×10^7 /μL with 0.020 vol % Triton X-100 solution. The spheres had a diameter of 2 μm and formed a closely packed hexagonal monolayer on the surface during air drying. The area that could be patterned with PS spheres depended on the concentration and total volume of the liquid solutions that were introduced onto the PDMS surface. Specifically, a circular coating with an approximately 1 cm diameter could be made by introducing a 30 μL volume suspension. The PDMS surface was indented by the PS spheres so as to create an asymmetric dimple array. We have previously demonstrated that by placing an array of PS spheres on a nascently prepared PDMS surface overnight, shallow and uniform dimples were formed in the elastomer.[52] This is most likely caused by the redistribution and cross-linking of uncured PDMS in the contact region between individual PS spheres and the PDMS surface. Here, we applied this idea to the creation of asymmetric features on the surface by tilting the PDMS substrate during the air drying and curing process. We dub this combination of oblique SAM deposition and surface indentation as oblique colloidal lithography. The process is described in detail below.

In the second step, the PS sphere-covered PDMS substrate was subjected to plasma etching (Figure 1B).[52] Reactive radicals produced from the reactive ion etchant (RIE), which contained CF_4 and O_2, were introduced vertically onto the PS sphere-covered PDMS surface. The asymmetric dimples from the previous step were located under the PS spheres and were not affected by the RIE process. The surface region that was not shielded, however, was etched. This led to a hexagonal array of PDMS pillars, which is commonly seen in conventional CL fabrications.[53] The etched portions of the PDMS surface corresponded to 3-fold hollow sites between the PS spheres. As a result, the surface PDMS patterns were composed of asymmetric dimples in the center surrounded by symmetric grooves. After the formation of a PDMS pattern, the PS spheres were dissolved away with toluene and the PDMS template was cleaned in acetone and water followed by drying at 130 °C for 30 min to remove any residual solvent. The resulting PDMS surface consisted of a hexagonal pillar array, whereby each pillar had an asymmetric dimple embeded on its top (Figure 1C). The morphology of the pillars could be tuned by the exact RIE time, the O_2 concentration, and the size of the PS spheres that were employed in the fabrication process. Moreover, the PDMS pillar array could easily be made to cover a square centimeter of surface area (Figure S1A).

Next, the PDMS template was pressed against a planar polystyrene surface and heated with an iron block (Figure 1D). To do this, the PDMS mold was mounted onto a polystyrene-coated planar glass substrate. An iron block was placed on top of the mold to ensure close contact between the mold and the polymer as well as to adjust the pressure applied to the substrate. The whole system was annealed for 1 h at 130 °C, which was above the glass transition temperature (T_g) for polystyrene.[54] This caused the asymmetric dimple feature to fill with melted PS, and ultimately the nonconcentric features as well as the pillar structures were embossed into the PS film (Figure 1E). Specifically, a polymer disk with an asymmetric height distribution was formed. The filling process was mainly driven by capillary action as the contact angle between the PDMS walls and the PS layer was initially 90°, which is far from the equilibrium contact angle.[48,55] These features remained in place in the PS film after the PDMS mold and iron block were removed at room temperature (Figure 1F).

In the next step, the PS patterns were transferred into an underlying gold layer through plasma etching (Figure 1G) and wet etching steps (Figure 1H). The perpendicular plasma etching speed was approximately 2 nm/s under 60 W RIE and a 20 standard cubic centimeters per minute (sccm) oxygen flow rate. Therefore, the amount of PS that was ultimately removed could be carefully controlled. After this, the partially exposed gold layer was then etched by immersing the chip into a 1:1 (volumetric) mixture of 50 mM ferric nitrate and 50 mM thiourea to conduct a wet chemical etch, leaving asymmetric Au patterns behind. The remaining PS layer was removed by toluene after gold etching (Figure 1H).

DOI: 10.1021/acsnano.6b07867
ACS Nano 2017, 11, 6594−6604

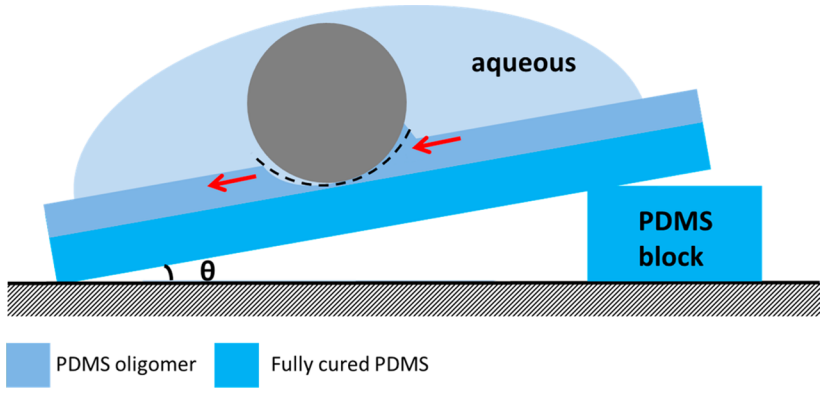

Figure 2. Schematic illustration of the formation of asymmetric PDMS dimples by oblique colloidal lithography.

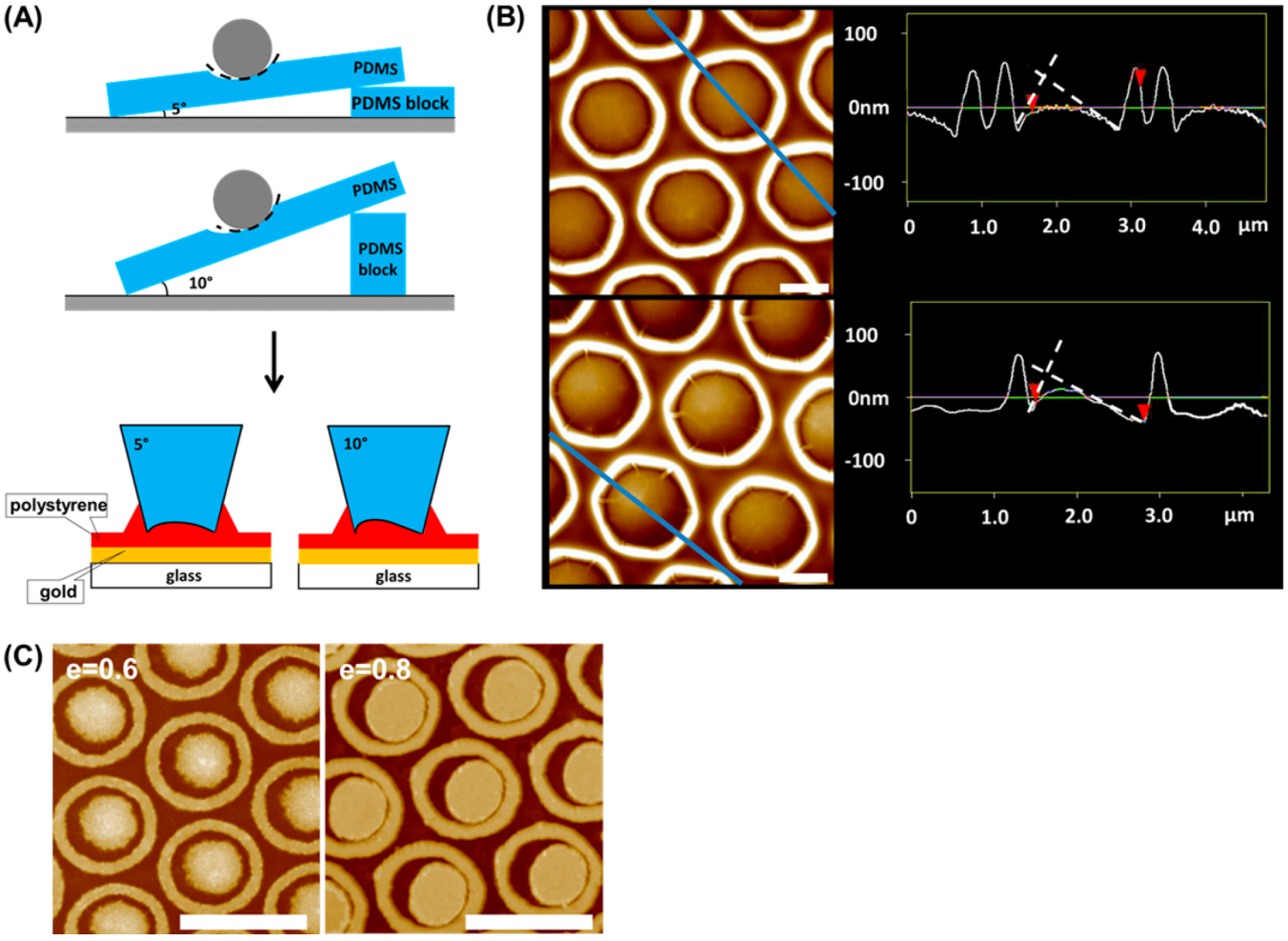

Figure 3. (A) Schematic illustration for the control of OCL asymmetry. (B) AFM images of PS features with two different eccentricity values obtained by imprinting 20 nm PS films at 130 °C for 1 h. Top: Small eccentricity (5°); bottom: large eccentricity (10°). Note the tilt angles are exaggerated in order to better show the difference. Scale bars: 1 μm. The PDMS templates were fabricated by 270 W RIE for 70 s in 35 sccm CF_4 and 5 sccm O_2. (C) As-prepared Au patterns obtained after 20 s of RIE of PS features in (B) followed by 9 min of wet etching. Scale bars: 2 μm.

Oblique Colloidal Lithography. As noted above, OCL is a more sophisticated version of conventional colloidal lithography that allows for the fabrication of asymmetric (especially nonconcentric) surface structures. It involves using a hydrophobic elastomer to assemble a PS sphere array and the creation of asymmetry features in an underlying template when using a tilted surface (Figure 2). Herein, PDMS was chosen as the substrate because dimples can be formed in it[52] and because it has well-understood properties.[56,57] Specifically, previous studies have demonstrated that there is a layer of silicone oligomers at the surface that is often not cured as well as the bulk PDMS.[52,58] In our experiment, the curing temperature and time were specifically chosen to ensure that the top layer of the PDMS slab was not fully cured. This layer of oligomers can

DOI: 10.1021/acsnano.6b07867
ACS Nano 2017, 11, 6594−6604

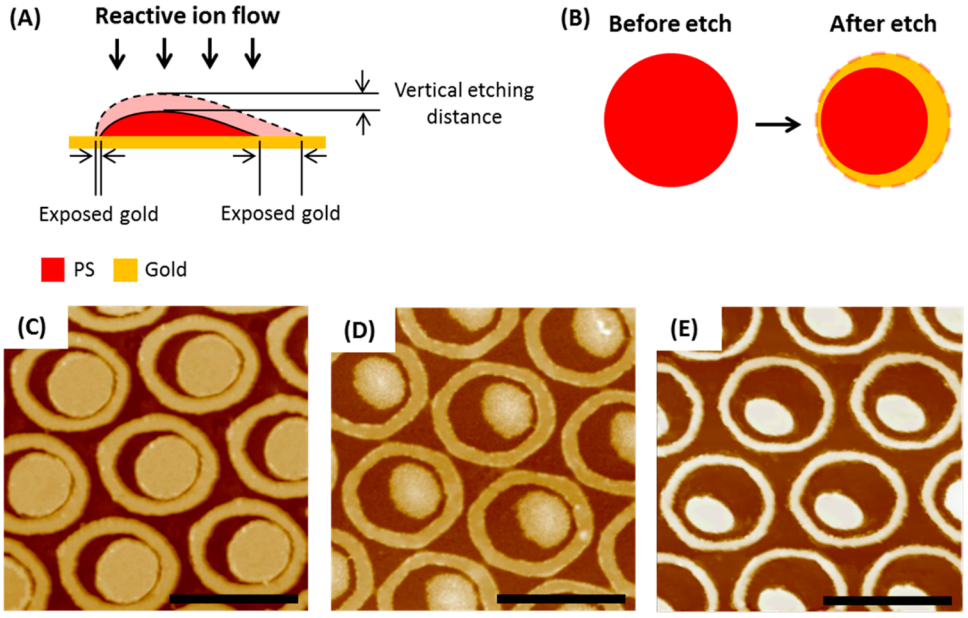

Figure 4. (A) Etching asymmetric PS patterns with RIE led to anisotropic exposure of the underlying gold layer; (B) top view schematic of the same process in (A); (C–E) gold features generated from the same PS patterns but with different RIE etch times. Specifically, the etch time was 20 s in (C), 30 s in (D), and 40 s in (E). Scale bars: 2 μm.

behave like a viscous liquid and redistribute under an external force. Generally, a symmetric dimple will be formed if the substrate plane lies normal to the direction of gravity (dashed curve in Figure 2). If the substrate is tilted, however, gravity can drive the PDMS oligomers toward the lower end of the indentation. In this case, PDMS oligomers pooling on one side would be in close contact with the PS bead, while the gap between the PDMS and PS sphere would be larger on the other side. Consequently, a distorted, asymmetric dimple can be formed on the tilted substrate. After further curing of the PDMS, an asymmetric dimple will be left behind upon the removal of the PS spheres (Figure S1B). It should be noted that only a limited range of tilt angles was possible with the current technique. Specifically, the procedure worked quite well for tilt angles of $\leq 10°$; however, when the tilt angle exceeded this value, the hexagonally ordered PS sphere array became disordered (Figure S2).

Feature Variety. By varying the parameters of the fabrication process, we were able to independently control the size, shape, and asymmetry of the nanostructures. In order to quantitatively describe the asymmetry of these structures, we defined a unitless parameter, eccentricity (e):

$$e = \sqrt{1 - \frac{b^2}{a^2}}$$

in which a and b represent the distance from the center of the inner disk to the two opposite centers of the outer ring along the direction of the asymmetry (Figure S3). The larger the value of e, the greater the asymmetry will be. Specifically, the value of e goes to 0 for spherically symmetric features and approaches 1 when the center of the inner disk is infinitely close to the edge of the outer ring.

The eccentricity showed an obvious correlation with the tilt angle of the PDMS substrate in OCL (Figure 3). As the redistribution of the interfacial PDMS oligomers was primarily driven by gravity, the shape of the asymmetric dimples could be readily tuned by adjusting the tilt angle, which led to differing values of e. As is shown schematically in Figure 3A, the difference in the tilt angle affected the asymmetry of the dimples. Specifically, the larger the angle, the larger the asymmetry was found to be. This translated into a height difference in the PDMS features as a function of angle as determined by atomic force microscopy (AFM) measurements (Figure 3B). Note that the outer ring in both patterns was found to be identical. This was expected, as it was molded by the symmetric grooves in the PDMS. As shown, PS patterns with $e = 0.6$ and $e = 0.8$ could be fabricated by using tilt angles of 5° and 10°, respectively. The gold features derived from these PS patterns after the wet etching process are shown in Figure 3C.

The geometry and size of the features in the final structures could be controlled by the size of the PS spheres that were employed, the RIE time, and the reaction conditions in CFL. In general, the size of each surface unit as well as its period was determined by the size of the PS spheres employed. Meanwhile, the gaps between the surface units that were critical to the optical properties of the products could be tuned by the RIE time. In RIE, a constant vertical etch rate was maintained. Since the thickness of the PS patterns was not a constant (*e.g.*, Figure 3B), the exposure of the underlying gold layer was highly dependent on the RIE time. Namely, for short etch times, only thinner portions of the PS patterns were completely removed, leaving a limited gold surface area accessible for the following wet etching step. On the other hand, a longer RIE time removed an ever wider area of the PS layer, leading in turn to the exposure of larger gold surface areas.

The asymmetric contour of PS patterns allowed for the creation of nonconcentric gold features (Figure 4). The thinner side of the asymmetric PS features was quickly removed, while the thicker side remained relatively intact (Figure 4A). As such, the RIE etching step led to an asymmetric exposure of the underlying gold layer (Figure 4B). The longer the etching time, the more prominent this became, provided that the PS film was not completely removed. As a result, nonconcentric gold

DOI: 10.1021/acsnano.6b07867
ACS Nano 2017, 11, 6594–6604

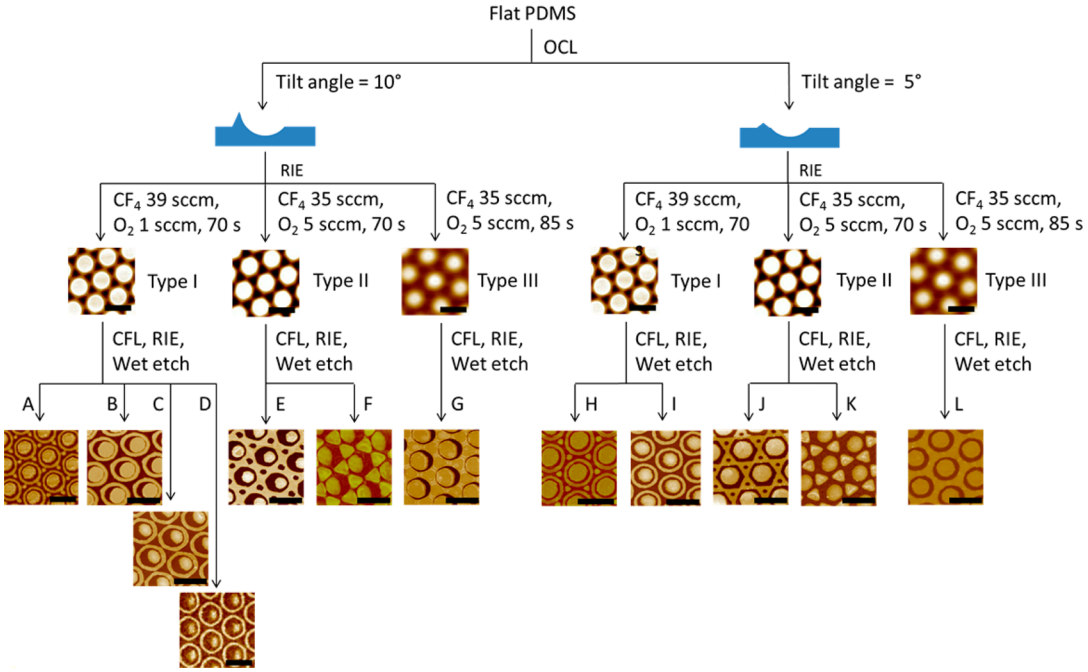

Figure 5. Branched tree guide to the parameters employed for fabricating various nonconcentric Au pattern motifs (A–L). Scale bars: 2 μm.

features could be fabricated by creating anisotropic gap sizes around the inner disk. Also, the size ratio between the inner and outer pattern could be tuned in a similar way. For example, the size of the inner disk was reduced dramatically by increasing the etching time, while that of the outer ring moiety changed more slowly. This difference in etch rates could also be attributed to the same mechanism. The ring feature possessed the highest height (Figure 4B), leading to the slowest removal rate. Consequently, extending the RIE time led to final products with significantly reduced inner disk size, but similar outer ring thicknesses (Figure 4C–E). On the other hand, the geometry of the outer PS patterns could be readily tuned by varying the morphology of the PDMS template or the thickness of the PS thin film layer, which helped to establish more distinctive patterns.[52]

Combining the methods described above, multiple types of nonconcentric features could be systematically fabricated as demonstrated by the branched tree guide shown in Figure 5. In the first step, the eccentricity was controlled by choosing the desired tilt angle in OCL. Specifically, a larger tilt angle of 10° (left branch) led to an eccentricity of e = 0.8, while a smaller tilt angle (5°) yielded e = 0.6 (right branch). Next, three types of PDMS templates for each e value were fabricated by tuning the etching time and the CF_4/O_2 levels in the RIE step. In general, higher CF_4 and O_2 flow rates as well as longer etching times resulted in better separated pillar arrays as opposed to less well separated pillars. We classified the interpillar spacing in the PDMS templates as types I, II, and III, which correspond to short, medium, and large interpillar spacing, respectively. Next, each type of PDMS template could be used to make multiple individually distinct gold patterns after employing the CFL, RIE, and wet chemical etching steps. For example, the thickness of the PS film in CFL played an important role in determining the morphology of patterns. When the type I PDMS template made from 10° tilt angle patterns was applied, a thinner PS film (30 nm) led to small dots surrounding target shapes (Figure 5A), while a thicker PS film (50 nm) resulted in targets only (Figure 5B–D). In the latter three cases, the RIE time was exploited to further tune the morphology of the patterned gold array. Specifically, as the RIE time increased, the gold patterns became thinner and smaller, but the overall geometry remained the same. Therefore, as the RIE time increased from 20 s (Figure 5B) to 30 s (Figure 5C) to 40 s (Figure 5D), a greater gap between the disk and the ring was created. The combination of a type II template made from a 10° tilt angle pattern and a 30 nm thick PS film yielded a dot-in-hexagram pattern (Figure 5E), while the combination of the same template and a 50 nm PS film yielded dots and triangles (Figure 5F). With a type III template made from a 10° tilt angle pattern and 50 nm PS film, a nonconcentric annular aperture array could be obtained (Figure 5G), which consisted of disks in the wells.

Gold patterns with analogous geometries but an eccentricity of 0.6 could be obtained by using a PDMS template made from 5° tilt angle patterns (Figure 5H–L). The specific conditions for each pattern are provided in Table 1. As can be seen from Figure 5, the sequential application of the independently controllable fabrication parameters led to a very large number of possible structures. The 12 representative gold nanopatterned arrays shown on the bottom of Figure 5 are provided in a larger format in Figure S4. This represents a wide variety of different and complex structures, including the dots-surrounded nonconcentric targets (Figure 5A and H), the nonconcentric hexagram disks (Figure 5E and J), and the nonconcentric annular aperture arrays (Figure 5G and L). In addition, it was possible to fabricate gaps down to 30 nm by tuning the plasma and wet etching times (Figure S5). The size of the smallest gaps was mainly limited by the lateral diffusion of the aqueous gold etchant in the chemical etching step. With the use of highly oriented gold etching methods, *e.g.*, RIE or ion milling, the fabrication of even smaller gaps should be possible.[59,60]

Optical Characterization. We have demonstrated the fabrication of libraries of nonconcentric patterns using OCL. Due to their asymmetric structures, we expected to see

DOI: 10.1021/acsnano.6b07867
ACS Nano 2017, 11, 6594–6604

Table 1. Patterning Conditions for Each Type of Polymer Feature

pattern[a]	polystyrene feature fabrication conditions[b]	plasma etching time	wet etching time	template fabrication conditions[c]
5A	30 nm, 1 h annealing	17 s	9 min	10°, CF_4 39 sccm, O_2 1 sccm, 270 W etch 70 s
5B	50 nm, 1 h annealing	20 s	9 min	10°, CF_4 35 sccm, O_2 5 sccm, 270 W etch 70 s
5C	50 nm, 1 h annealing	30 s	9 min	10°, CF_4 35 sccm, O_2 5 sccm, 270 W etch 70 s
5D	50 nm, 1 h annealing	40 s	9 min	10°, CF_4 35 sccm, O_2 5 sccm, 270 W etch 70 s
5E	30 nm, 1 h annealing	20 s	10 min	10°, CF_4 35 sccm, O_2 5 sccm, 270 W etch 70 s
5F	50 nm, 1 h annealing	25 s	9 min	10°, CF_4 35 sccm, O_2 5 sccm, 270 W etch 70 s
5G	50 nm, 1 h annealing	35 s	11 min	10°, CF_4 35 sccm, O_2 5 sccm, 270 W etch 85 s
5H	30 nm, 1 h annealing	17 s	9 min	5°, CF_4 39 sccm, O_2 1 sccm, 270 W etch 70 s
5I	50 nm, 1 h annealing	20 s	9 min	5°, CF_4 35 sccm, O_2 5 sccm, 270 W etch 70 s
5J	30 nm, 1 h annealing	20 s	10 min	5°, CF_4 35 sccm, O_2 5 sccm, 270 W etch 70 s
5K	50 nm, 1 h annealing	25 s	9 min	5°, CF_4 35 sccm, O_2 5 sccm, 270 W etch 70 s
5L	50 nm, 1 h annealing	35 s	11 min	5°, CF_4 35 sccm, O_2 5 sccm, 270 W etch 85 s

[a]The patterns are listed by the figure number they appeared in. [b]The temperature was 130 °C. [c]The first number indicates the tilt angle in the OCL process.

interesting features in their optical spectra, such as multiple plasmonic modes and Fano resonances that would be of great promise in future sensing applications. To test our assumption, extinction spectra of a nonconcentric annular aperture array (nAAA) were recorded (Figure 6A), whose structure was identical to that in Figure 5G. We selected this pattern because the coupling between the disk and well should be strong due to the narrow gap width (~30 nm) between them. Extraordinary transmission has been reported for annular aperture arrays (AAAs).[61−63] Similarly, we also observed an extraordinary optical transmission at ~1560 nm (a dip in the extinction) for an nAAA with unpolarized light. Interestingly, one additional dip could be found at ~1820 nm, which was polarization dependent and became more obvious under 0° polarization. The asymmetric contours of the two dips indicate that they should likely originate from Fano resonances. In addition, three distinct peaks located at 1750, 1900, and 2700 nm were found in the extinction spectra, which presumably correspond to a high-order multipolar mode, an antibonding dipolar mode, and a bonding dipolar mode, respectively (Figure 6A, blue spectrum). Note that the higher noise level on the longer wavelength end of the experimental spectra was due to the elevated thermal background at longer wavelengths. Additional experiments with polarized light show that the intensities of all three peaks are polarization dependent. Specifically, when the polarized incident beam was parallel to the direction of pattern deviation, the three peaks became clearer with a relatively deeper dip at ~1820 nm (red spectrum). In the case of the 90° polarized excitation, the 1750 and 1900 nm peaks moved closer together, which weakened the extinction dip at ~1820 nm (green spectrum). Moreover, the peak at 2700 nm disappeared at 90°, demonstrating the anisotropic optical properties of the nonconcentric structures. This phenomenon originated from the polarization-dependent electronic coupling between the structural units.

To corroborate the spectra shown in Figure 6A, we carried out finite-difference time-domain (FDTD) simulations.[64] Simulated model dimension parameters were set based on the experimental AFM images. The approach distance between

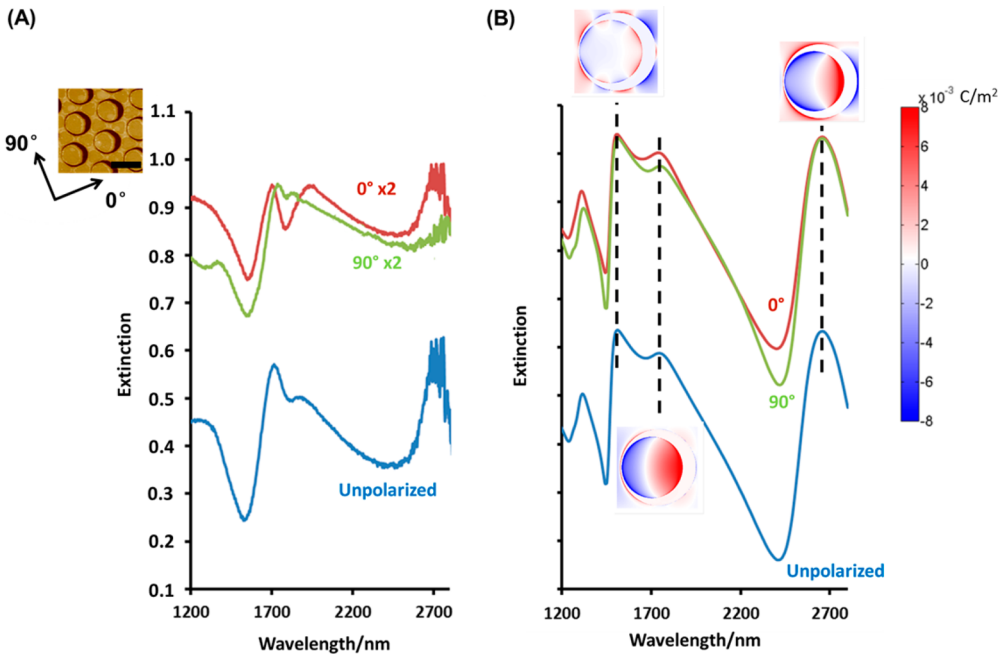

Figure 6. Experimental and calculated extinction spectra of a nonconcentric annular aperture array. (A) Experimental extinction spectra of a nonconcentric annular aperture array obtained with unpolarized light (blue spectrum) and with polarized light at 0° and 90° excitation (red and green spectra, respectively). Scale bar: 2 μm. (B) Extinction spectra of a nonconcentric annular aperture array obtained by FDTD calculations. Insets: Charge distribution profiles for the corresponding resonances.

DOI: 10.1021/acsnano.6b07867
ACS Nano 2017, 11, 6594−6604

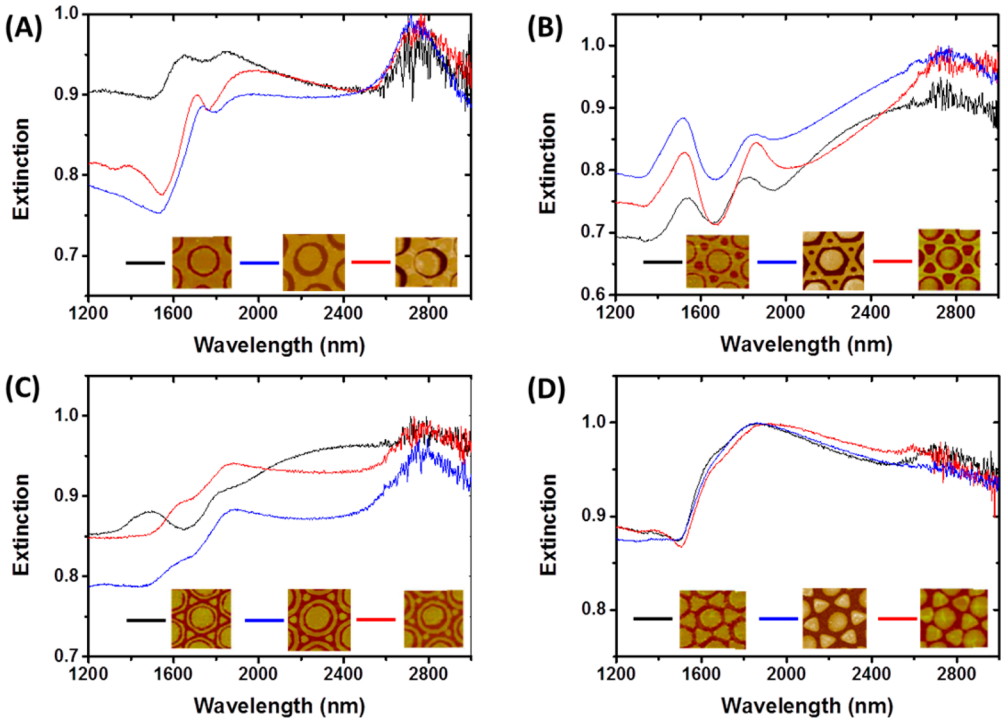

Figure 7. Influence of asymmetry on the extinction spectra of (A) annular apertures, (B) hexgram-dot patterns, (C) triangle-target patterns, and (D) triangle-dot patterns. The extinction spectra were generated at three different eccentricity values: e = 0 (black curves), e = 0.6 (blue spectra), and e = 0.8 (red spectra).

the inner disk and the outer hole was 30 nm. Three major peaks and two extraordinary optical transmissions were observed in the simulated extinction spectra (Figure 6B). Their positions were qualitatively in agreement with the experimental results. These calculations confirmed that the pronounced asymmetric extinction dip around 1500 nm was a Fano resonance caused by the multipolar SPR mode. Another dip presented at 1820 nm in the experimental spectra was also a Fano resonance, as verified by FDTD simulations. This assignment is based on the charge plot and also on the simple standing wave model as noted in a previous publication.[64] A bonding dipolar mode peak and other higher order mode peaks appear separately in the spectra from the mid-infrared to the near-infrared range. As can be seen, there are some differences between the simulations and the experimental results. This could occur for several reasons. First, there can be defects in individual features and the two-dimensional domain sizes are finite with boundaries between individual domains. Also, it should be noted that the gold films in the samples consisted of tiny gold grains, rather than a continuous single crystal as assumed in the simulation. Extinction spectra for additional gold features, including the nonconcentric triangle-targets and nonconcentric hexagram-disks, are provided in the Supporting Information (Figure S6). FDTD simulations have also been included. The results demonstrated that symmetry breaking could lead to multipolar modes and Fano resonances in the spectra.

Introducing eccentricity should play a critical role in the optical absorbance of numerous gold features. To demonstrate this, we compared the experimental spectra of nonconcentric patterns with the corresponding concentric ones in four different cases. In each case, the extinction spectrum was determined for e = 0, e = 0.6, and e = 0.8. It was found that for apertures (Figure 7A) and hexagram-disk patterns (Figure 7B), the extinction spectra changed notably after introducing asymmetry. Specifically, the peak profile became asymmetric after introducing eccentricity, which should be due to the generation of Fano resonances. The greater the eccentricity was, the more obvious this phenomenon generally became. On the other hand, the nonconcentric triangle-target pattern exhibited overlapping peaks compared with its symmetric counterpart (Figure 7C). This demonstrated that symmetry breaking might also weaken the coupling between plasmonic structures for certain geometries. Also, the extinction spectra of the asymmetric triangle-dot pattern showed only a slight variation compared to its symmetric counterpart (Figure 7D). A very small new peak at ~1420 nm and a lower dip near ~1510 nm were seen for e = 0.8, while most of the spectral profile looked similar regardless of asymmetry. These results clearly indicate that symmetric breaking, especially eccentricity, can change the optical properties of plasmonic structures in many different ways depending on the geometry. Our fabrication technique should be useful in helping to sort out rules for understanding what changes can be expected.

Finally, it should be noted that the as-fabricated nonconcentric patterns have stable optical properties regardless of the direction in which the substrate is tilted. We have conducted FDTD simulations to confirm this, which have been included in the Supporting Information (Figure S7).

CONCLUSIONS

In summary, we have developed a stepwise strategy to establish libraries of asymmetric, nonconcentric plasmonic structures. The approach used here combined colloidal lithography, reactive ion etching, and capillary force lithography. A wide variety of polystyrene and Au patterns could be fabricated on the micro- and nanoscales, with surface elements as small as tens of nanometers. Complex features, such as asymmetric

DOI: 10.1021/acsnano.6b07867
ACS Nano 2017, 11, 6594−6604

hexagonal webs and targets with triangles, could be created by simply choosing a proper combination of templating and etching conditions. The same features would be extremely challenging and time-consuming to generate by other methods. The optical characterization of nonconcentric plasmonic structures demonstrated that the asymmetric features we have fabricated possessed polarization-dependent optical properties. FDTD simulations confirmed that the spectral peaks from these features originated from dipolar and multipolar SPR modes of the nonconcentric gold features.

This strategy affords an inexpensive and relatively simple means to form asymmetric nanopatterned structures compared with e-beam lithography. It could be further applied to create surface patterns with different materials by combining it with other chemical and lithographic processes. For example, nanopatterned semiconductor crystals could be created *via* drop casting for nanoscale optoelectronic applications.[65] In addition, the optical absorption features of nonconcentric patterns possess great promise in developing the next generation of SPR sensors, photocatalysts, and optical devices.

METHODS

Oblique Colloidal Lithography. Polystyrene beads of certified size standards were purchased from Duke Scientific Corporation with diameters of 2 μm. The beads were centrifuged five times with copious amounts of water to remove surfactants and other impurities that were present. They were then redissolved in purified water (Barnstead nanopure water system, 18 MΩ/cm resistivity). The concentration of PS spheres was maintained at $4 \times 10^7/\mu$L. Triton X-100, laboratory grade, was purchased from Sigma-Aldrich. PS bead suspensions were mixed with a 0.1% (volume percentage) Triton X-100 solution in a 4:1 ratio to yield a final surfactant concentration of 0.020 vol %. PDMS molds were made by mixing Sylgard 184 silicone elastomer with 10 wt % of the Sylgard 184 curing agent. The mixture was cured at 70 °C for 3 h. Before introducing the aqueous PS sphere suspension, the PDMS surface was treated with an 18 W oxygen plasma for 15 s to increase its hydrophilicity. The PDC-32G plasma cleaner/sterilizer was from Harrick Plasma (Ithaca, NY, USA). The PDMS substrate was tilted by inserting a PDMS wedge of desired size under one of its edges. Two tilt angles, namely 5° and 10°, were applied. The angles were measured by a protractor.

PDMS Templates. A March CS-1701 reactive ion etcher was used to create PDMS templates. To do this, a PDMS film coated with a monolayer of PS spheres was exposed to a CF_4/oxygen plasma at 270 W in the reactive ion etcher for varying time periods. The total flow rate of the etchant was kept at 40 sccm, while the etchant composition was varied for creating different surface morphologies. After treatment, the polystyrene spheres were removed from the PDMS surface by washing with toluene and acetone. Toluene was bought from EMD, and acetone was purchased from Fisher Scientific. Both were ACS grade. The cleaned PDMS template was incubated at 130 °C for 30 min in order to remove any remaining solvent.

Polystyrene and Au Features. Glass slides (VWR, No. 2 micro cover slides) were treated with piranha solution to remove organics from the surface. This solution was a 3:1 mixture of sulfuric acid (EMD, ACS grade) and hydrogen peroxide (Acros Organics, 35%) (*caution: piranha solutions are extremely corrosive, reactive, and potentially explosive and need to be handled with care in a fume hood*). The glass slides were then washed with water and baked in an oven (Orton, Sentry Xpress 2.0) at 500 °C for 5 h. A 50-nm-thick Au layer (Alfa Aesar, 99.999%) was thermally evaporated onto the glass slides using a 5-nm-thick chromium layer as an adhesive. This was done in a BOC Edwards metal evaporator (Auto 360). Polystyrene powder (Scientific Polymer, MW = 97 400) was first dissolved in toluene and then spin-coated onto the planar Au surface using a WS-400B-6NPP/LITE spin coater (Laurell Techonologies Corporation). The spin rate was set to 3000 rpm, while the concentration of the PS solution was tuned between 5 and 25 mg/mL, depending on the thickness of the PS film that was desired.

The PDMS template was placed on a polymer layer, and an iron block was used to adjust the applied pressure. The applied pressure was set to $\sim 7.9 \times 10^3$ Pa by placing an 80 g iron block on a 1 cm by 1 cm PDMS mold. Next, the system was annealed at 130 °C for 1 h and then cooled to room temperature in air. After peeling away the PDMS layer, the nascently formed polymer features were treated in an oxygen plasma to completely remove desired portions of the PS film. The power of the RIE was set to 60 W, and the oxygen flow rate was 20 sccm, which initially corresponded to a removal rate of ~2 nm/s. Finally, the whole chip was immersed in a mixture of 50 mM iron nitrate (Alfa Aesar, 98+%) and 50 mM thiourea (Alfa Aesar, 99%). After removing the unprotected Au, the chip was rinsed with purified water and treated with chromium etchant 1020AC (Transene Company Inc.) for 1 min to dissolve the exposed chromium. The remaining PS layer was removed by toluene before each gold feature was examined by AFM (Digital Instrument, multimode scanning probe microscope) in tapping mode to explore the surface topography.

Extinction Spectroscopy. Extinction spectra in the visible−NIR range were recorded by a Hitachi 4100 UV−vis−NIR spectrometer. Glass slides (VWR, No. 2 micro cover slides) were treated with piranha solution to remove organics from the surface. This solution was a 3:1 mixture of sulfuric acid (EMD, ACS grade) and hydrogen peroxide (Acros Organics, 35%) (*caution: piranha solutions are extremely corrosive, reactive, and potentially explosive and need to be handled with care in a fume hood*). The glass slides were then washed with water and baked in an oven (Orton, Sentry Xpress 2.0) at 500 °C for 5 h before use as references in spectral measurements. Each spectrum was recorded from 400 to 3000 nm at a speed of 750 nm/min from 850 to 3000 nm and 600 nm/min for wavelengths below 850 nm. The optical slit was fixed at 2 nm below 850 nm and autochanged in the 850 to 3000 nm region to achieve optimized sensitivity. In order to investigate the effect of polarization on the nonconcentric nanofeatures, a polarizer was inserted in the light path in front of the sample.

Simulations. The commercial software FDTD Lumerical 7.5.3 was used to calculate the extinction spectra of the nanostructures. Periodic boundary conditions were set in the $x-y$ plane, and perfect matched layer boundary conditions were applied in the z-direction to eliminate numerical artifacts at the simulation boundary. For gold permittivity, we used literature values.[66] The gold nanostructures were supported by a semi-infinite silica substrate. The unit cell for each periodic array was defined within the simulation domain, and a normalized incident plane wave was inserted in accordance with the experimental configuration. The electric field of the polarized light was defined in such a way that its orientation was parallel (0°) or perpendicular (90°) to the offset of the inner disk. Next, a 2D($x-y$ plane) infinity monitor was placed below the sample in order to record the transmission. The extinction spectra were calculated from the transmission spectra. The procedure was repeated over a set of wavelengths to compile a full extinction spectrum.

ASSOCIATED CONTENT

Supporting Information

The Supporting Information is available free of charge on the ACS Publications website at DOI: 10.1021/acsnano.6b07867.

Information on the effects of various parameters on OCL and the fabrication of nonconcentric features; extinction spectra of additional nonconcentric gold patterns (PDF)

AUTHOR INFORMATION

Corresponding Author

*E-mail (P. S. Cremer): psc11@psu.edu.

ORCID

Zhi Zhao: 0000-0002-4491-7641

Peter Nordlander: 0000-0002-1633-2937

DOI: 10.1021/acsnano.6b07867
ACS Nano 2017, 11, 6594−6604

Paul S. Cremer: 0000-0002-8524-0438

Notes

The authors declare no competing financial interest.

ACKNOWLEDGMENTS

This work was supported by a Norman Hackerman Advanced Research Project Program grant (010366-0040-2009) and the Office of Naval Research (N00014-08-0467). P.N. acknowledges support from the Robert A. Welch Foundation under grant C-1222.

REFERENCES

(1) Ebbesen, T. W.; Lezec, H. J.; Ghaemi, H. F.; Thio, T.; Wolff, P. A. Extraordinary Optical Transmission Through Sub-wavelength Hole Arrays. *Nature* **1998**, *391*, 667−669.

(2) Joannopoulos, J. D.; Johnson, S. G.; Winn, J. N.; Meade, R. D. *Photonic Crystals: Molding the Flow of Light*; Princeton University Press: Princeton, 1995.

(3) Miguez, H.; Meseguer, F.; Lopez, C.; Mifsud, A.; Moya, J. S.; Vazquez, L. Evidence of FCC Crystallization of SiO_2 Nanospheres. *Langmuir* **1997**, *13*, 6009−6011.

(4) Jacobs, H. O.; Whitesides, G. M. Submicrometer Patterning of Charge in Thin-film Electrets. *Science* **2001**, *291*, 1763−1766.

(5) Thurn-Albrecht, T.; Schotter, J.; Kästle, G. A.; Emley, N.; Shibauchi, T.; Krusin-Elbaum, L.; Guarini, K.; Black, C. T.; Tuominen, M. T.; Russell, T. P. Ultrahigh-density Nanowire Arrays Grown in Self-assembled Diblock Copolymer Templates. *Science* **2000**, *290*, 2126−2129.

(6) Ostuni, E.; Chen, C. S.; Ingber, D. E.; Whitesides, G. M. Selective Deposition of Proteins and Cells in Arrays of Microwells. *Langmuir* **2001**, *17*, 2828−2834.

(7) Haes, A. J.; Van Duyne, R. P. A Nanoscale Optical Biosensor: Sensitivity and Selectivity of an Approach Based on the Localized Surface Plasmon Resonance Spectroscopy of Triangular Silver Nanoparticles. *J. Am. Chem. Soc.* **2002**, *124*, 10596−10604.

(8) Lee, K. B.; Park, S. J.; Mirkin, C. A.; Smith, J. C.; Mrksich, M. Protein Nanoarrays Generated by Dip-pen Nanolithography. *Science* **2002**, *295*, 1702−1705.

(9) Kohli, P.; Harrell, C. C.; Cao, Z.; Gasparac, R.; Tan, W.; Martin, C. R. DNA-Functionalized Nanotube Membranes with Single-base Mismatch Selectivity. *Science* **2004**, *305*, 984−986.

(10) Bruchez, M.; Moronne, M.; Gin, P.; Weiss, S.; Alivisatos, A. P. (1998). Semiconductor Nanocrystals as Fluorescent Biological Labels. *Science* **1998**, *281*, 2013−2016.

(11) Gao, X.; Cui, Y.; Levenson, R. M.; Chung, L. W.; Nie, S. *In Vivo* Cancer Targeting and Imaging with Semiconductor Quantum Dots. *Nat. Biotechnol.* **2004**, *22*, 969−976.

(12) Link, S.; El-Sayed, M. A. Size and Temperature Dependence of the Plasmon Absorption of Colloidal Gold Nanoparticles. *J. Phys. Chem. B* **1999**, *103*, 4212−4217.

(13) Xu, H.; Bjerneld, E. J.; Käll, M.; Börjesson, L. Spectroscopy of Single Hemoglobin Molecules by Surface Enhanced Raman Scattering. *Phys. Rev. Lett.* **1999**, *83*, 4357.

(14) Xu, H.; Aizpurua, J.; Käll, M.; Apell, P. Electromagnetic Contributions to Single-Molecule Sensitivity in Surface-enhanced Raman Scattering. *Phys. Rev. E: Stat. Phys., Plasmas, Fluids, Relat. Interdiscip. Top.* **2000**, *62*, 4318.

(15) Gao, H.; McMahon, J. M.; Lee, M. H.; Henzie, J.; Gray, S. K.; Schatz, G. C.; Odom, T. W. Rayleigh Anomaly-surface Plasmon Polariton Resonances in Palladium and Gold Subwavelength Hole Arrays. *Opt. Express* **2009**, *17*, 2334−2340.

(16) Fedotov, V.; Rose, M.; Prosvirnin, S.; Papasimakis, N.; Zheludev, N. Sharp Trapped-Mode Resonances in Planar Metamaterials with a Broken Structural Symmetry. *Phys. Rev. Lett.* **2007**, *99*, 147401.

(17) Zheludev, N. I.; Prosvirnin, S. L.; Papasimakis, N.; Fedotov, V. A. Lasing spaser. *Nat. Photonics* **2008**, *2*, 351−354.

(18) Verellen, N.; Sonnefraud, Y.; Sobhani, H.; Hao, F.; Moshchalkov, V. V.; Van Dorpe, P.; Nordlander, P.; Maier, S. A. Fano Resonances in Individual Coherent Plasmonic Nanocavities. *Nano Lett.* **2009**, *9*, 1663−1667.

(19) Chu, M. W.; Myroshnychenko, V.; Chen, C. H.; Deng, J. P.; Mou, C. Y.; García de Abajo, F. J. Probing Bright and Dark Surface-plasmon Modes in Individual and Coupled Noble Metal Nanoparticles Using an Electron Beam. *Nano Lett.* **2008**, *9*, 399−404.

(20) Nordlander, P.; Oubre, C.; Prodan, E.; Li, K.; Stockman, M. I. Plasmon Hybridization in Nanoparticle Dimers. *Nano Lett.* **2004**, *4*, 899−903.

(21) Hu, C.; Liu, L.; Zhao, Z.; Chen, X.; Luo, X. Mixed Plasmons Coupling for Expanding the Bandwidth of Near-perfect Absorption at Visible Frequencies. *Opt. Express* **2009**, *17*, 16745−16749.

(22) Ding, P.; Liang, E.; Cai, G.; Hu, W.; Fan, C.; Xue, Q. Dual-band Perfect Absorption and Field Enhancement by Interaction between Localized and Propagating Surface Plasmons in Optical Metamaterials. *J. Opt.* **2011**, *13*, 075005.

(23) Luk'yanchuk, B.; Zheludev, N. I.; Maier, S. A.; Halas, N. J.; Nordlander, P.; Giessen, H.; Chong, C. T. The Fano Resonance in Plasmonic Nanostructures and Metamaterials. *Nat. Mater.* **2010**, *9*, 707−715.

(24) Zhang, S.; Bao, K.; Halas, N. J.; Xu, H.; Nordlander, P. Substrate-induced Fano Resonances of a Plasmonic Nanocube: a Route to Increased-sensitivity Localized Surface Plasmon Resonance Sensors Revealed. *Nano Lett.* **2011**, *11*, 1657−1663.

(25) Hao, F.; Sonnefraud, Y.; Van Dorpe, P.; Maier, S. A.; Halas, N. J.; Nordlander, P. Symmetry Breaking in Plasmonic Nanocavities: Subradiant LSPR Sensing and a Tunable Fano Resonance. *Nano Lett.* **2008**, *8*, 3983−3988.

(26) Cetin, A. E.; Altug, H. Fano Resonant Ring/disk Plasmonic Nanocavities on Conducting Substrates for Advanced Biosensing. *ACS Nano* **2012**, *6*, 9989−9995.

(27) Waldeisen, J. R.; Wang, T.; Ross, B. M.; Lee, L. P. Disassembly of a Core-satellite Nanoassembled Substrate for Colorimetric Biomolecular Detection. *ACS Nano* **2011**, *5*, 5383−5389.

(28) Zhang, S.; Genov, D. A.; Wang, Y.; Liu, M.; Zhang, X. Plasmon-induced Transparency in Metamaterials. *Phys. Rev. Lett.* **2008**, *101*, 047401.

(29) Chang, W. S.; Lassiter, J. B.; Swanglap, P.; Sobhani, H.; Khatua, S.; Nordlander, P.; Halas, N. J.; Link, S. A Plasmonic Fano Switch. *Nano Lett.* **2012**, *12*, 4977−4982.

(30) Rechberger, W.; Hohenau, A.; Leitner, A.; Krenn, J. R.; Lamprecht, B.; Aussenegg, F. R. Optical Properties of Two Interacting Gold Nanoparticles. *Opt. Commun.* **2003**, *220*, 137−141.

(31) Grand, J.; Adam, P. M.; Grimault, A. S.; Vial, A.; Lamy de la Chapelle, M.; Bijeon, J. L.; Kostcheev, S.; Royer, P. Optical Extinction Spectroscopy of Oblate, Prolate and Ellipsoid Shaped Gold Nanoparticles: Experiments and Theory. *Plasmonics* **2006**, *1*, 135−140.

(32) Duan, H.; Hu, H.; Kumar, K.; Shen, Z.; Yang, J. K. W. Direct and Reliable Patterning of Plasmonic Nanostructures with Sub-10-nm Gaps. *ACS Nano* **2011**, *5*, 7593−7600.

(33) Mukherjee, S.; Sobhani, H.; Lassiter, J. B.; Bardhan, R.; Nordlander, P.; Halas, N. J. Fanoshells: Nanoparticles with Built-in Fano Resonances. *Nano Lett.* **2010**, *10*, 2694−2701.

(34) Zhu, F. Q.; Chern, G. W.; Tchernyshyov, O.; Zhu, X. C.; Zhu, J. G.; Chien, C. L. Magnetic Bistability and Controllable Reversal of Asymmetric Ferromagnetic Nanorings. *Phys. Rev. Lett.* **2006**, *96*, 027205.

(35) Haynes, C. L.; Van Duyne, R. P. Nanosphere Lithography: a Versatile Nanofabrication Tool for Studies of Size-dependent Nanoparticle Optics. *J. Phys. Chem. B* **2001**, *105*, 5599−5611.

(36) Duval Malinsky, M.; Kelly, K. L.; Schatz, G. C.; Van Duyne, R. P. Nanosphere Lithography: Effect of Substrate on the Localized Surface Plasmon Resonance Spectrum of Silver Nanoparticles. *J. Phys. Chem. B* **2001**, *105*, 2343−2350.

(37) Per Hanarp, M. K.; Sutherland, D. S. Optical Properties of Short Range Ordered Arrays of Nanometer Gold Disks Prepared by Colloidal Lithography. *J. Phys. Chem. B* **2003**, *107*, 5768−5772.

DOI: 10.1021/acsnano.6b07867
ACS Nano 2017, 11, 6594−6604

(38) Fredriksson, H.; Alaverdyan, Y.; Dmitriev, A.; Langhammer, C.; Sutherland, D. S.; Zäch, M.; Kasemo, B. Hole-mask Colloidal Lithography. *Adv. Mater.* **2007**, *19*, 4297−4302.
(39) McLellan, J. M.; Geissler, M.; Xia, Y. Edge Spreading Lithography and its Application to the Fabrication of Mesoscopic Gold and Silver Rings. *J. Am. Chem. Soc.* **2004**, *126*, 10830−10831.
(40) Liao, W. S.; Chen, X.; Chen, J.; Cremer, P. S. Templating Water Stains for Nanolithography. *Nano Lett.* **2007**, *7*, 2452−2458.
(41) Sun, Z.; Li, Y.; Zhang, J.; Li, Y.; Zhao, Z.; Zhang, K.; Zhang, G.; Guo, J.; Yang, B. A Universal Approach to Fabricate Various Nanoring Arrays Based on a Colloidal-crystal-assisted-lithography Strategy. *Adv. Funct. Mater.* **2008**, *18*, 4036−4042.
(42) Chen, J.; Liao, W. S.; Chen, X.; Yang, T.; Wark, S. E.; Son, D. H.; Batteas, J. D.; Cremer, P. S. Evaporation-induced Assembly of Quantum Dots into Nanorings. *ACS Nano* **2009**, *3*, 173−180.
(43) Lu, Y.; Yin, Y.; Xia, Y. Preparation and Characterization of Micrometer-sized "Egg Shells. *Adv. Mater.* **2001**, *13*, 271−274.
(44) Chen, K.; Rajeeva, B. B.; Wu, Z.; Rukavina, M.; Dao, T. D.; Ishii, S.; Aono, M.; Nagao, T.; Zheng, Y. Moiré Nanosphere Lithography. *ACS Nano* **2015**, *9*, 6031−6040.
(45) Nemiroski, A.; Gonidec, M.; Fox, J. M.; Jean-Remy, P.; Turnage, E.; Whitesides, G. M. Engineering Shadows to Fabricate Optical Metasurfaces. *ACS Nano* **2014**, *8*, 11061−11070.
(46) Zhao, J.; Frank, B.; Burger, S.; Giessen, H. Large-area High-quality Plasmonic Oligomers Fabricated by Angle-controlled Colloidal Nanolithography. *ACS Nano* **2011**, *5*, 9009−9016.
(47) Vogel, N.; Fischer, J.; Mohammadi, R.; Retsch, M.; Butt, H. J.; Landfester, K.; Weiss, C. K.; Kreiter, M. Plasmon Hybridization in Stacked Double Crescents Arrays Fabricated by Colloidal Lithography. *Nano Lett.* **2011**, *11*, 446−454.
(48) Suh, K. Y.; Kim, Y. S.; Lee, H. H. Capillary Force Lithography. *Adv. Mater.* **2001**, *13*, 1386.
(49) Deegan, R. D.; Bakajin, O.; Dupont, T. F.; Huber, G.; Nagel, S. R.; Witten, T. A. Capillary Flow as the Cause of Ring Stains from Dried Liquid Drops. *Nature* **1997**, *389*, 827−829.
(50) Deegan, R. D. Pattern Formation in Drying Drops. *Phys. Rev. E: Stat. Phys., Plasmas, Fluids, Relat. Interdiscip. Top.* **2000**, *61*, 475−485.
(51) Deegan, R. D.; Bakajin, O.; Dupont, T. F.; Huber, G.; Nagel, S. R.; Witten, T. A. Contact Line Deposits in an Evaporating Drop. *Phys. Rev. E: Stat. Phys., Plasmas, Fluids, Relat. Interdiscip. Top.* **2000**, *62*, 756−765.
(52) Zhao, Z.; Cai, Y.; Liao, W. S.; Cremer, P. S. Stepwise Molding, Etching, and Imprinting to Form Libraries of Nanopatterned Substrates. *Langmuir* **2013**, *29*, 6737−6745.
(53) Cheung, C. L.; Nikolić, R. J.; Reinhardt, C. E.; Wang, T. F. Fabrication of Nanopillars by Nanosphere Lithography. *Nanotechnology* **2006**, *17*, 1339−1343.
(54) Glocker, D. A.; Shah, S. I. *Handbook of Thin Film Process Technology*; Taylor & Francis: Abingdon, 1995.
(55) Cai, Y.; Zhao, Z.; Chen, J.; Yang, T.; Cremer, P. S. Deflected Capillary Force Lithography. *ACS Nano* **2012**, *6*, 1548−1556.
(56) Xia, Y.; Kim, E.; Zhao, X. M.; Rogers, J. A.; Prentiss, M.; Whitesides, G. M. Complex Optical Surfaces Formed by Replica Molding against Elastomeric Masters. *Science* **1996**, *273*, 347−349.
(57) Anderson, J. R.; Chiu, D. T.; Wu, H.; Schueller, O. J.; Whitesides, G. M. Fabrication of Microfluidic Systems in Poly (dimethylsiloxane). *Electrophoresis* **2000**, *21*, 27−40.
(58) Yunus, S.; de Looringhe, C. D.; Poleunis, C.; Delcorte, A. Diffusion of Oligomers from Polydimethylsiloxane Stamps in Microcontact Printing: Surface Analysis and Possible Application. *Surf. Interface Anal.* **2007**, *39*, 922−925.
(59) Green, T. A. Gold Etching for Microfabrication. *Gold Bull.* **2014**, *47*, 205−216.
(60) Kollmann, H.; Piao, X.; Esmann, M.; Becker, S. F.; Hou, D.; Huynh, C.; Kautschor, L.; Bösker, G.; Vieker, H.; Beyer, A.; Gölzhäuser, A.; Park, N.; Vogelgesang, R.; Silies, M.; Gölzhäuser, A. Toward Plasmonics with Nanometer Precision: Nonlinear Optics of Helium-Ion Milled Gold Nanoantennas. *Nano Lett.* **2014**, *14*, 4778−4784.
(61) Perentes, A.; Utke, I.; Dwir, B.; Leutenegger, M.; Lasser, T.; Hoffmann, P.; Baida, F.; Bernal, M. P.; Russey, M.; Salvi, J.; Van Labeke, D. Fabrication of Arrays of Sub-wavelength Nano-apertures in an Optically Thick Gold Layer on Glass Slides for Optical Studies. *Nanotechnology* **2005**, *16*, S273.
(62) Poujet, Y.; Salvi, J.; Baida, F. I. 90% Extraordinary Optical Transmission in the Visible Range through Annular Aperture Metallic Arrays. *Opt. Lett.* **2007**, *32*, 2942−2944.
(63) Poujet, Y.; Roussey, M.; Salvi, J.; Baida, F. I.; Van Labeke, D.; Perentes, A.; Santschi, C.; Hoffmann, P. Super-transmission of Light through Subwavelength Annular Aperture Arrays in Metallic Films: Spectral Analysis and Near-field Optical Images in the Visible Range. *Photonics and Nanostructures-Fundamentals and Applications* **2006**, *4*, 47−53.
(64) Cai, Y.; Cao, Y.; Nordlander, P.; Cremer, P. S. Fabrication of Split-rings *via* Stretchable Colloidal Lithography. *ACS Photonics* **2014**, *1*, 127−134.
(65) Mentzel, T. S.; Wanger, D. D.; Ray, N.; Walker, B. J.; Strasfeld, D.; Bawendi, M. G.; Kastner, M. A. Nanopatterned Electrically Conductive Films of Semiconductor Nanocrystals. *Nano Lett.* **2012**, *12*, 4404−4408.
(66) Palik, E. D. *Handbook of Optical Constants of Solids*; Academic Press: New York, 1985.

DOI: 10.1021/acsnano.6b07867
ACS Nano 2017, 11, 6594−6604